

Shape Sensing of Continuum Robots using Direct Laser Writing

Amber K. Rothe*, *Graduate Student Member, IEEE*, Nidhi Malhotra, *Graduate Student Member, IEEE*,
and Jaydev P. Desai, *Fellow, IEEE*

Abstract—Continuum robots offer a promising approach for minimally invasive and natural-orifice surgical procedures due to their inherent compliance and dexterity. However, this flexibility also makes estimating the current shape of the robot challenging. Several approaches have been used to reconstruct the shape of these robots, including imaging, optical sensing, magnetic sensing, and resistive sensing. Strain sensors fabricated using direct laser writing (DLW) could provide an alternative sensing method. This technique involves using a laser to induce carbonization of certain polymers to create graphene patterns, such as strain sensors. In this paper, we demonstrate how a flexible continuum joint and a DLW sensor can be machined as one monolithic structure using the same laser and the same setup. The fabricated sensors are characterized using linear and nonlinear models, which are used to predict the joint angle with error as low as 1.76° . Furthermore, we demonstrate how a DLW sensor can be used to implement closed-loop control in a robotic joint, achieving tracking error under 3° .

I. INTRODUCTION

Continuum robots are a promising approach for minimally invasive surgery due to their flexibility and dexterity. However, their inherent compliance makes pose estimation challenging, and it remains an active area of research, where many approaches have been proposed [1], [2]. Imaging-based methods generally have been used successfully for shape feedback [1]; however, due to the slow scan speed of magnetic resonance imaging [3], low resolution and high noise of ultrasound [1], and radiation risk associated with fluoroscopy [1], safely and reliably achieving a sampling frequency sufficient for closed-loop control with imaging methods is challenging. Another common approach for pose estimation relies on electromagnetic sensors [4], [5]. However, other electronics in the operating room can interfere with these sensors [1], [2]. Furthermore, optical sensors such as fiber Bragg gratings have been used to detect the strain in continuum robots [6], [7], but they are fragile and expensive. Resistive sensors, which transduce bending strain as resistance change, can take various forms [2]. Some works incorporate off-the-shelf strain sensors in continuum robotic actuators to obtain shape feedback [8], [9]. Other works incorporate carbon-filled polymer coatings to create strain sensors [10], [11]. Another approach involves encapsulating conductive liquid, such as gallium-indium ink, in a narrow channel [12], [13]. However, the use of resistive strain

sensors for continuum robot shape sensing involves several challenges. Many fabrication approaches require multiple fabrication and assembly steps to create the sensor itself and integrate it with the robot [14], resulting in high costs and a high likelihood of errors during the assembly procedures. Additionally, miniaturizing the strain sensors sufficiently to allow integration with slender continuum robots such as catheters and guidewires is an open problem [15].

One promising method for fabricating strain sensors is direct laser writing (DLW), wherein a laser is used to create patterns of conductive graphene on certain polymer materials such as polyimide [16]–[19]. In prior work, DLW was used to fabricate strain sensors on commercial polyimide tape and which were incorporated with nitinol-based continuum robotic joints [20]. The approach allowed both the DLW sensors and the notched tube continuum robotic joints to be manufactured using the same laser micromachining system. The fabrication did not use expensive materials or additional equipment. However, this approach still required assembling the sensor on the robotic tool body, which was time-consuming and provided an opportunity for errors. In another work, it was shown that tubes made of polyimide can be used to fabricate tendon-driven notched-tube style robotic joints [21]. In this work, we combine these approaches, fabricating DLW strain sensors directly on the robot body, then cutting the notches on the same machine without changing the setup. This approach streamlines the fabrication process and eliminates assembly errors due to misalignment of the sensor. In addition, the present work characterizes the DLW sensors more thoroughly, investigating effects such as hysteresis, rate dependence, and relaxation which were not considered in [20]. To our knowledge, this is the first attempt to fabricate a DLW sensor directly on a robotic tool. In this paper, we present the following contributions:

- A novel process for fabricating DLW strain sensors on the outside surface notched-tube continuum robotic joints using one machining setup and leaving the central lumen open.
- A detailed characterization of the proposed sensor-integrated robot (sensing joint) investigating hysteresis, sensor response rate-dependence, and joint relaxation.
- An assessment of the proposed sensors' accuracy for estimating the bending angle of the sensing joints, using joints with one or multiple sensors.
- A closed-loop control scheme incorporating the sensor feedback from the proposed approach to track the bending angle of the robotic joint.

Research reported in this publication was supported in part by Developmental Funds from the Winship Cancer Institute of Emory University.

The authors are with the Medical Robotics and Automation (RoboMed) Laboratory, Wallace H. Coulter Department of Biomedical Engineering, Georgia Institute of Technology, Atlanta, GA 30332 USA (*A. K. Rothe is the corresponding author. Email: amber.rothe@gatech.edu).

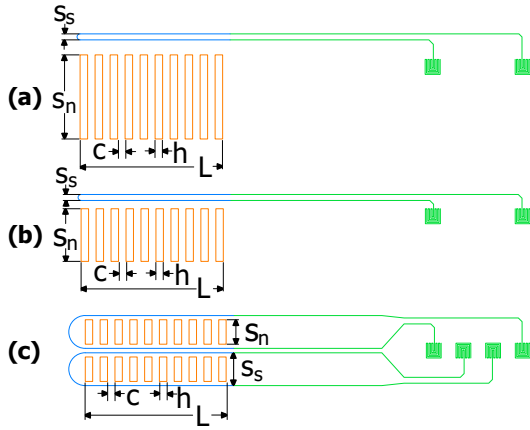


Fig. 1. Schematic showing the design for (a) Joint A, (b) Joint B, and (c) Joint C. The notches are shown in orange, the strain gauge in blue, and the leads and contact pads in green.

TABLE I
DESIGN PARAMETERS

	Joint A	Joint B	Joint C
Notch Style	UAN	UAN	BSN
Outer Radius, r_o	1.24 mm	0.800 mm	0.800 mm
Inner Radius, r_i	0.875 mm	0.610 mm	0.610 mm
Notch Circumference, s_n	5.61 mm	3.52 mm	1.65 mm \times 2
Notch Width, h	0.500 mm	0.500 mm	0.500 mm
Notch Spacing, c	0.500 mm	0.500 mm	0.500 mm
Number of Notches, N	10	10	10 \times 2
Joint Length, L	9.5 mm	9.5 mm	9.5 mm
Sensor Circumference, s_s	0.400 mm	0.400 mm	2.13 mm \times 2

This paper is organized as follows: Section II outlines the design and fabrication of the sensing joints. Section III describes the models used to characterize the sensor. Section IV details the experiments, results, and discussion pertaining to the characterization and validation of the sensors. Conclusions and future work are discussed in Section V.

II. METHODS

A. Design

Three sensing joints were designed to be fabricated from stock polyimide tubing (MicroLumen, Oldsmar, FL, USA). Two were unidirectional asymmetric notch (UAN) joints with a single sensor along the unnotched backbone. The other joint was a bidirectional symmetric notch (BSN) joint with two sensors between the notches. The sensors terminated in square spirals to provide large contact pads for connecting additional electronics. Both the sensing element and notches for each joint were designed in the same AutoCAD file (Autodesk, San Francisco, CA, USA). The dimensions of Joint A, Joint B, and Joint C are given in Table I and shown in Fig. 1(a), Fig. 1(b), and Fig. 1(c), respectively.

B. Fabrication

1) *Laser Micromachining*: A piece of machine steel of diameter 1.2 mm or 1.5 mm was placed inside the 1.6 mm or 2.5 mm outer diameter stock polyimide tubing (Fig. 2(a)), respectively, to increase the stiffness of the polymer tubes

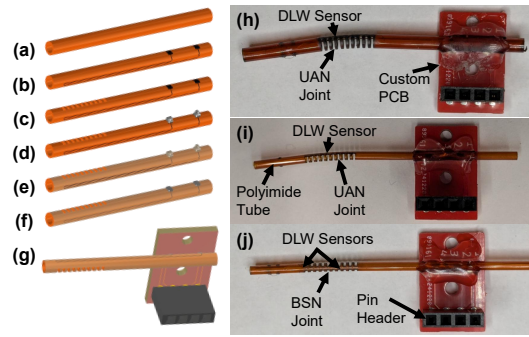


Fig. 2. The sensing joint fabrication process (a) begins with stock polyimide tubing. (b) A laser is used to draw the sensor on the tube and (c) cut notches in the tube. (d) The contact pads are protected by silver epoxy before (e) the entire structure is coated with parylene-C. (f) The parylene is sanded off the contact pads, and (g) additional silver epoxy is used to assemble the sensing joint with the PCB. The images of the completed sensing joints: (h) Joint A, (i) Joint B, and (j) Joint C.

TABLE II
LASER PARAMETERS

	(a) Sensor	(b) Notches
Wavelength, λ	1030 nm	1030 nm
Power, P	160 mW	2.00 W
Scan Speed, v	1.00 mm s ⁻¹	25 mm s ⁻¹
Pulse Frequency, f	200 kHz	60 kHz
Pulse Width, t_p	550 fs	215 fs
Repetitions, n_{rep}	1	32

during the machining process and secured on one end using a small amount of cyanoacrylate glue. The stock was then fixtured in the femtosecond laser micromachining system (WS-Flex Ultra-Short Pulse Laser Workstation, Optec, Frameries, Belgium), with the right end secured in the collet of the system's rotation stage and the left end resting in a custom 3D-printed jig. The overall parameters of the laser system used are given in Table II. Parameters were selected for fabricating the sensor and notches based on previous work [20], [21], as well as calibration of the laser. First, the sensing elements were machined using the settings given in Table II, column (a) (Fig. 2(b)). Then, without changing the laser setup, the notches were machined using the settings given in Table II, column (b) (Fig. 2(c)). Finally, a clean cut was made to separate the sensing joint from the remainder of the tube using the same settings. Fabricating both the sensor and the notches using the same equipment and setup eliminates the possibility of human error in aligning or assembling the sensor with the notches.

2) *Protection of the Contact Pads*: To protect the contact pads during the subsequent steps of the process, a small amount of conductive silver epoxy (8331D, MG Chemicals, Burlington, ON, Canada) was placed on each contact pad and allowed to cure overnight (Fig. 2(d)).

3) *Parylene Coating*: To seal the sensor and protect it during use, the joints were coated with parylene-C (Galentis, Venice, Italy). A Labcoater PDS 2010 (Specialty Coating Systems, Indianapolis, IN, USA) was used to perform the vacuum deposition of 8 g of parylene, for a nominal expected

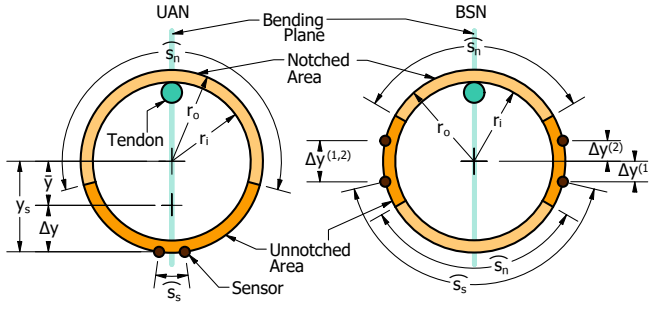


Fig. 3. Schematic of the notch cross section for UAN and BSN designs.

thickness of approximately $5\ \mu\text{m}$ (Fig. 2(e)).

4) *PCB Assembly*: The parylene coating was carefully sanded off of the protected contact pads using a small file (Fig. 2(f)). Then, additional silver epoxy was used to attach the contact pads to a custom printed circuit board (PCB), which provided female pin connections for wiring the sensor to the other system electronics (Fig. 2(g)). A custom 3D-printed jig was used to align the contact pads on the sensing joint with the contact pads on the PCB. The epoxy was allowed to dry overnight. Finally, hot melt adhesive was used to improve the mechanical connection between the joint and the PCB, as the epoxy provides a strong electrical connection but a weak mechanical connection. The three designed joints, Joint A, Joint B, and Joint C, are shown in Fig. 2(h), Fig. 2(i), and Fig. 2(j), respectively.

5) *System Assembly*: A nylon tendon of diameter $0.28\ \text{mm}$ (OmniFlex 8lb, Zebco, Tulsa, OK, USA) was affixed to the distal end of the sensing joint. The sensing joint-PCB assembly was clamped firmly with screws to the actuation system, while the tendon was attached to a lead screw actuated by a DC motor. The sensors were attached to a simple voltage divider circuit, with the output connected to a data acquisition board (National Instruments, Austin, TX, USA). The constant resistor in the voltage divider circuit had a measured resistance of $99.6\ \text{k}\Omega$. For Joint C, which had two sensors, the value of the second resistor was $102.5\ \text{k}\Omega$. An electromagnetic (EM) tracker (Northern Digital Inc. Aurora, Waterloo, ON, Canada) was placed in the tip of the sensing joint to provide ground-truth deflection angle data. All data during the experiments was collected at $500\ \text{Hz}$.

III. CALCULATIONS AND MODELING

A. Strain

The strain, ε , experienced in the sensor due to a joint deflection of angle θ can be calculated using the geometry of the joint. It is assumed that bending in the unnotched sections is negligible [22]. The perpendicular distance between the sensors and the center of the tube, y_s , is given by:

$$y_s = r_o \cos(\phi_s/2), \quad \text{where} \quad \phi_s = s_s/r_o \quad (1)$$

where s_s is the circumferential distance between the arms of the sensor and r_o is the outer radius of the tube. The distance between the neutral plane and the center of the tube,

\bar{y} (Fig. 3), depends on the UAN or BSN notch style [20]:

$$\bar{y}_A = \bar{y}_B = \frac{4 \sin(\pi - s_n/(2r_o)) (r_o^3 - r_i^3)}{3 (2\pi - s_n/r_o) (r_o^2 - r_i^2)}, \quad \bar{y}_C = 0 \quad (2)$$

where r_i is the inner radius of the tube and s_n is the arc length of the notch. The strain in the sensor, ε , is given by:

$$\varepsilon = (\Delta y \theta) / L, \quad \Delta y = y_s - \bar{y} \quad (3)$$

where Δy is the distance between the neutral plane and the plane of the sensor.

B. Sensor Resistance

A voltage divider circuit is used to obtain the sensor readings. When the sensed voltage is V , the input voltage is V^+ , and the known resistor has a resistance of R_k , the resistance in the sensor, R is given by:

$$R = R_k / ((V^+ / V) - 1) \quad (4)$$

C. Linear Model

A simple linear model has been used to characterize DLW strain gauges in the literature [23], [24]. In such models, the gauge factor, GF, is used to express how resistance, R , changes in response to strain, ε , and is defined by [25]:

$$\text{GF} = (R - R_0) / (R_0 \varepsilon) \quad (5)$$

where R_0 is the initial resistance of the unstrained gauge and R is the resistance associated with strain ε . Re-arranging this equation yields the forward and inverse relationship between strain and sensor resistance, given by:

$$R = R_0 \text{GF} \varepsilon + R_0, \quad \varepsilon = (R - R_0) / (R_0 \text{GF}) \quad (6)$$

In a joint with two strain gauges of gauge factors $\text{GF}^{(1)}$ and $\text{GF}^{(2)}$ and initial resistances of $R_0^{(1)}$ and $R_0^{(2)}$, the deflection angle can be estimated independently from each gauge using the above equations. Alternatively, the deflection angle may be calculated from both gauges, where $R^{(1)}$ and $R^{(2)}$ are the resistance of each gauge and $\Delta y^{(1,2)}$ is the distance between the planes of the gauges (Fig. 3):

$$\theta = \frac{L}{\Delta y^{(1,2)}} \left(\frac{R^{(2)} - R_0^{(2)}}{R_0^{(2)} \text{GF}^{(2)}} - \frac{R^{(1)} - R_0^{(1)}}{R_0^{(1)} \text{GF}^{(1)}} \right) \quad (7)$$

D. Prandtl-Ishlinskii Model

Other works have noted that the relationship between strain and resistance for DLW sensors may not be linear, and have modeled it using various piecewise linear [26], [27], and quadratic [28] models. In this work, we propose using the generalized Prandtl-Ishlinskii (PI) hysteresis model [29] to represent the relationship between strain and sensor resistance. The PI model is capable of capturing both non-linearity and hysteresis. The forward model estimates the sensor resistance, $R(t)$, given the sensor strain, $\varepsilon(t)$ through time, t . The PI model used in this work is based on the play operator, $\Gamma_\rho(\nu(t))$, given by [29]:

$$\Gamma_\rho(\nu(t)) = \max(\nu(t) - \rho, \min(\nu(t) + \rho, \Gamma_\rho(\nu(t-1)))) \quad (8)$$

with the initial condition given by:

$$\Gamma_\rho(\nu(0)) = \max(\nu(0) - \rho, \min(\nu(0) + \rho, M_0)) \quad (9)$$

Where ρ is the radius of the play operator, t is time, M_0 is the initial value, and $\nu(t)$ is the input to the play operator.

The PI model allows the play operator to be combined with a function that modifies its shape. If the data appears to saturate, a hyperbolic tangent function is a good choice for this. Thus, the input to the play operator for the forward model is the hyperbolic tangent of the strain:

$$\nu(\varepsilon(t)) = \begin{cases} a_1 \tanh(a_2 \varepsilon(t) + a_3) + a_4, & \varepsilon(t) \geq \varepsilon(t-1) \\ a_5 \tanh(a_6 \varepsilon(t) + a_7) + a_8, & \varepsilon(t) < \varepsilon(t-1) \end{cases} \quad (10)$$

where a_j , $j = \{1, 2, \dots, 8\}$ are constants. The expected sensor resistance is computed as a weighted sum of N play operators, with weights P_i and radii ρ_i , $i = \{1, 2, \dots, N\}$, where R_c and ε_c are constants, given by:

$$R(t) = \sum_{i=1}^N P_i \Gamma_{\rho_i}(\nu(\varepsilon(t) - \varepsilon_c)) + R_c \quad (11)$$

The inverse model estimates the sensor strain, $\varepsilon(t)$, given the measured sensor resistance, $R(t)$. The inverse PI model incorporates another PI model of order N [29], [30]:

$$\varepsilon(t) = \nu^{-1} \left(\sum_{i=1}^N Q_i \Gamma_{\zeta_i}(R(t) - R_c) \right) + \varepsilon_c \quad (12)$$

where the radii, ζ_i , $i = \{1, 2, \dots, N\}$, and the weights Q_i , $i = \{1, 2, \dots, N\}$, are given by:

$$\begin{aligned} \zeta_i &= \sum_{j=1}^i P_j (\rho_i - \rho_j), & Q_1 &= 1/P_1 \\ Q_i &= -P_i / \left((P_1 + \sum_{j=1}^i P_j) (P_1 + \sum_{j=1}^{i-1} P_j) \right) \end{aligned} \quad (13)$$

and $\nu^{-1}(\mu(t))$ is the inverse of the hyperbolic tangent function for input $\mu(t)$, given by:

$$\nu^{-1}(\mu(t)) = \begin{cases} \frac{1}{a_2} \left(\operatorname{atanh} \left(\frac{1}{a_1} (\mu(t) - a_4) \right) - a_3 \right), & \mu(t) \geq \mu(t-1) \\ \frac{1}{a_6} \left(\operatorname{atanh} \left(\frac{1}{a_5} (\mu(t) - a_8) \right) - a_7 \right), & \mu(t) < \mu(t-1) \end{cases} \quad (14)$$

IV. EXPERIMENTS AND RESULTS

Several experiments were conducted to characterize the behavior and performance of the sensing joints, such as the hysteresis of the sensor, rate dependence of the sensor, and relaxation of the joint. The models described in Section III were fit to the experimental data and used to perform closed-loop control during the joint's motion. Finally, a demonstration of a sensing joint in a hydrogel phantom was performed to show the feasibility of the proposed approach in a physiological environment.

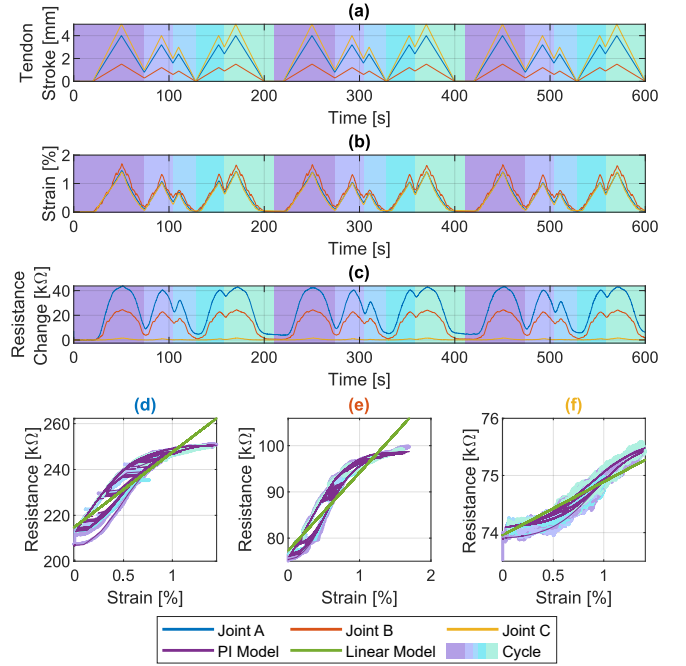


Fig. 4. Data for the sensor characterization experiment. (a) The tendon stroke pattern. This pattern was repeated five times in the experiment. (b) The strain, calculated from the ground truth angle. (c) The change in sensor resistance, calculated from the sensor voltage. The relationship between sensor resistance and strain for (d) Joint A, (e) Joint B, and (f) Joint C. Each distinct loading/unloading cycle is shaded in a different color.

A. Sensor Characterization

1) *Resistance-Strain Relationship*: To characterize the relationship between resistance change and strain for the three joints, the tendon was pulled and released with the profile shown in Fig. 4(a), consisting of five cycles of different amplitudes. The ground truth sensor deflection angle was recorded using the electromagnetic tracker, and the strain at the sensor was calculated using Eq. (3), shown in Fig. 4(b). Overall, the range of strains tested was between 0% and approximately 1.5%, which corresponded to about 26°, 58°, and 40° bending in Joints A, B, and C, respectively. For Joint C, which has two sensors, only the sensor in tension is considered in this section. The other sensor is considered in Section IV-B.2. The sensor voltage was also recorded, and its resistance calculated using Eq. (4) is shown in Fig. 4(c). For this and the other experiments, all input signals were filtered with moving average filters of 500 samples. This is relatively aggressive filtering intended to counter the high noise observed in the system signals. In future work, other noise mitigation strategies may be attempted. A simple linear best-fit model for the resistance-strain relationship was found using regression. The gauge factor and initial resistance (intercept) are shown in Table III.

We observed that the gauge factor for Joint C is lower than the others, indicating that the sensor on Joint C is less sensitive. Joint A and Joint B have unidirectional notches, allowing the sensor to be placed very close to the plane of bending (Fig. 3). On the other hand, Joint C has symmetrical notches, thus the sensors must be placed nearly 90° around the tube from the bending plane (Fig. 3). We hypothesize that

TABLE III
ANGLE ESTIMATION PARAMETERS

		Joint A	Joint B	Joint C
Linear Model	GF	15.3	22.0	1.28
	R_0	215 k Ω	77.2 k Ω	74.0 k Ω
PI Model	R_c	224 k Ω	87.9 k Ω	74.7 k Ω
	ε_c	0.307 %	0.531 %	0.804 %
	m_c	5136 k Ω	3090 k Ω	181 k Ω
	R_{peak}	250 k Ω	99.2 k Ω	754 k Ω
	$\varepsilon_{\text{peak}}$	1.35 %	1.57 %	1.37 %

this difference causes the large variation in gauge factor between the two designs. The change in resistivity of graphene is related to microscopic cracking of the conductive network [31]. In the BSN design, the graphene is constrained by the adjacent raw polyimide as it bends nearly tangentially to the surface of the tube. However, the sensor in the UAN design bends nearly orthogonally to the tube's surface; therefore, the graphene network is unconstrained, allowing larger cracks to form in the graphene network. Future research will be necessary to fully understand the phenomenon.

Although the linear model may be adequate for some applications, the relationship between resistance and strain is both hysteretic and nonlinear. Therefore, the PI model discussed in Section III-D was fit to the data. The order was chosen to be $N = 10$. The N radii, ρ_i were chosen to be evenly spaced from 0 to ρ_{max} . Because the PI model discussed in Section III-D is centered around the origin, it was first necessary to shift the data to center it on the origin. The resistance at the center, R_c , was estimated as the resistance where the slope of the resistance-strain plot was greatest during the loading phase of the first cycle, with a value of m_c . The strain at the center, ε_c , was estimated as the mean of the corresponding strain in the loading phase of the first cycle and the unloading phase of the last cycle. The weights, P_i , and constants, a_j , were chosen using nonlinear optimization. Because the optimization was highly sensitive to its initial conditions, a good starting "guess" of these values was necessary. The initial weights, $P_i^{(0)}$ and initial constants, $a_j^{(0)}$, as well as ρ_{max} , are given by:

$$\begin{aligned}
 a_1^{(0)} &= a_5^{(0)} = R_{\text{peak}} - R_c \\
 a_2^{(0)} &= a_6^{(0)} = m_c / (2(R_{\text{peak}} - R_c)) \\
 a_3^{(0)} &= a_4^{(0)} = a_7^{(0)} = a_8^{(0)} = 0 \\
 P_i^{(0)} &= (R_{\text{peak}} - R_c) / N, i = 1, 2, \dots, N \\
 \rho_{\text{max}} &= a_1^{(0)} \tanh(a_2^{(0)} \varepsilon_{\text{peak}} + a_3^{(0)}) + a_4^{(0)}
 \end{aligned} \tag{15}$$

The PI model is shown in a purple color while the linear model is shown in a green color in Fig. 4(d), Fig. 4(e), and Fig. 4(f) for Joint A, Joint B, and Joint C, respectively. Selected model parameters are given in Table III.

2) *Rate Dependence of Sensor Response*: Some polymeric materials exhibit rate-dependent behavior [32]; therefore, it was important to determine if the sensor's response is affected by the speed of the joint's actuation. To this end, the tendon of each joint was pulled and released with the profile shown in Fig. 5(a), consisting of five cycles. The amplitude

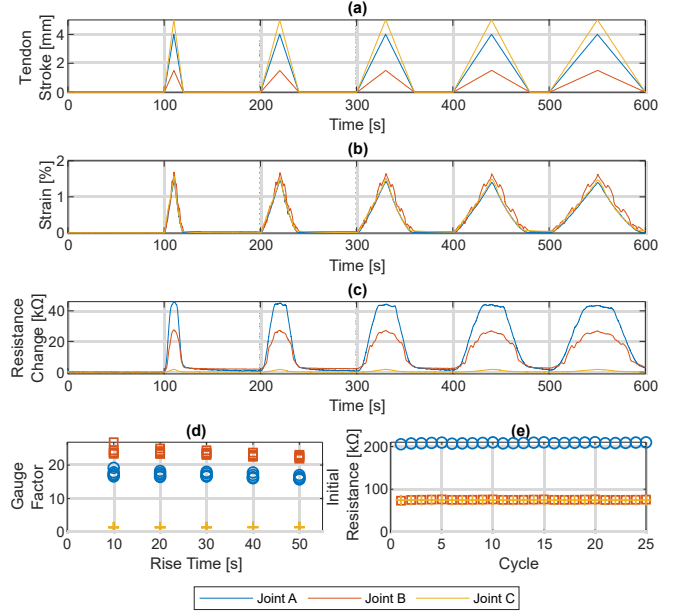


Fig. 5. Data for the rate-dependence experiment. (a) The tendon stroke pattern, featuring five cycles of loading and unloading with identical amplitude but different rise and fall times. (b) The strain, calculated from the ground truth measured angle. (c) The change in sensor resistance, calculated from the measured sensor voltage. (d) The linear gauge factor, GF, of each cycle, plotted against the rise time for that cycle (e) The initial resistance, R_0 , of each cycle, plotted against the cycle number.

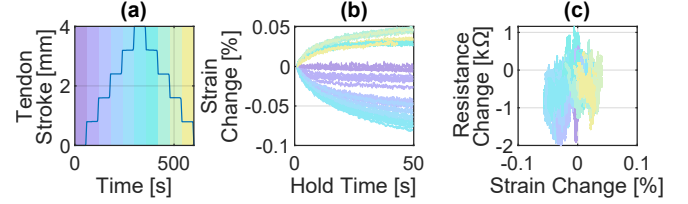


Fig. 6. Data for the relaxation experiment for Joint A. (a) The tendon stroke pattern, featuring stepwise loading and unloading. This pattern was repeated five times in the experiment (b) The decay in strain during each period of constant tendon stroke. (c) The relationship between resistance and strain during each period of constant tendon stroke.

of the tendon stroke was the same for each cycle; however, the duration of the tendon stroke was varied between 10 s and 50 s to achieve a variation in stroke speed. The cycles were repeated five times over a total time of 3000 s. The sensor strain and resistance were obtained as in Section IV-A.1 and shown in Fig. 5(b) and Fig. 5(c), respectively. For each cycle, the linear gauge factor was determined by fitting the linear model to each individual cycle, and plotted in Fig. 5(d). The correlation coefficient between stroke duration and gauge factor was calculated to be 0.0062, 0.0010, and 0.0011 for Joint A, Joint B, and Joint C, respectively, indicating low correlation between speed and sensor response.

In addition, the initial resistance of each cycle, R_0 , which is the intercept of the linear model, is plotted Fig. 5(e). The standard deviation of the initial resistance values was calculated to be 1.10 k Ω , 0.596 k Ω , and 0.038 k Ω for Joint A, Joint B, and Joint C, respectively, indicating that the drift in the sensor across the 25 total cycles was low.

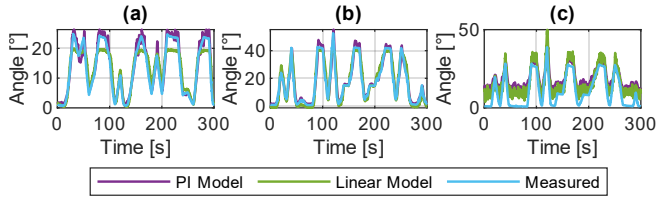


Fig. 7. The ground truth angle and the angle estimated using the linear and PI models for (a) Joint A, (b) Joint B, and (c) Joint C.

TABLE IV
ANGLE ESTIMATION RESULTS

	Joint A	Joint B	Joint C
Linear	2.76°	3.51°	5.25°
PI	1.76°	2.65°	7.57°

3) *Relaxation*: In another experiment, the tendon stroke was held constant at various amplitudes, shown in Fig. 6(a) for Joint A. This stroke pattern was repeated five times over 3000s while the strain and sensor resistance were recorded. It was observed that when the tendon stroke was held constant for a time, the joint angle and therefore calculated strain changed, presumably due to viscoelastic properties in the polymer tube and polymer tendon (Fig. 6(b)). However, during this time, the change in sensor resistance (Fig. 6(c)) was small and not strongly correlated to the change in strain, with a correlation coefficient of 0.118. Thus, the proposed sensor may be inadequate for capturing viscoelastic behavior and may need to be used in conjunction with other sensing methods when these effects are expected to be significant.

B. Angle Estimation

1) *Angle Estimation with One Sensor*: The inverse linear and PI models for the three joints were calculated based on the forward models determined in Section IV-A.1 according to Section III-C and Section III-D, respectively. The tendon was actuated in a randomly generated pattern, which was repeated for a total of 3000s. The recorded sensor resistance was used to predict the strain using each of the inverse models. Because the atanh function has asymptotic behavior, extrapolating beyond the range of the original data collected is unlikely to be accurate. Therefore, all resistances above and below this range were replaced with the maximum and minimum resistance observed during the sensor characterization experiment performed in Section IV-A.1 for the PI model prediction. Then, the expected joint angle was calculated using Eq. (3). Because the atanh function is very steep near its asymptotes, the model is highly sensitive to small changes in resistance. Therefore, the predicted angles were filtered aggressively with a moving average filter of 1000 samples. The ground truth angle, linear model predicted angle, and PI model predicted angle for Joint A, Joint B, and Joint C are shown in Fig. 7(a), Fig. 7(b), and Fig. 7(c), respectively. The root mean square errors (RMSE) between the predicted and actual angles are recorded in Table IV. The PI model was more accurate for Joint A and B, while the linear model remained more accurate for Joint C. As previously discussed, Joint C is also the least sensitive potentially due to the

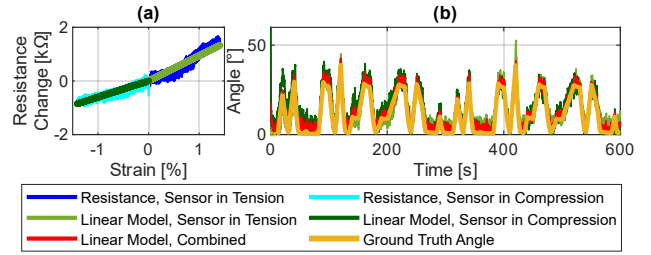


Fig. 8. (a) The modeled and actual resistance versus strain for the sensor in tension and compression. (b) The ground truth and estimated angle based on the sensor in tension, the sensor in compression, and both.

TABLE V
TWO SENSOR MODEL PARAMETERS

	Gauge Factor (GF)	Initial Resistance (R_0)	Correlation Coefficient (r^2)
Sensor in Tension	1.28	74.0 kΩ	0.888
Sensor in Compression	0.680	88.9 kΩ	0.892

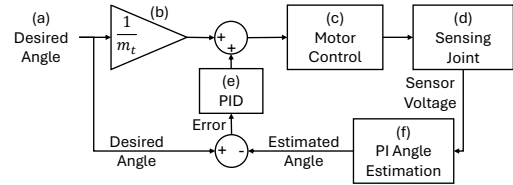


Fig. 9. Closed-loop control system for Joint D. (a) Desired angle input. (b) Tendon stroke-joint angle model. (c) Low level motor control. (d) Physical sensing joint. (e) PID controller. (f) Angle estimation subsystem.

difference in the direction of the graphene cracking; it is observed that in this configuration, the hysteric and saturating behavior captured by the PI model is less significant.

2) *Angle Estimation with Two Sensors*: In the case where there are two sensors on the same joint, as in Joint C, which has the BSN design shown in Fig. 3, it is possible to combine the readings from both sensors to obtain a more accurate and robust estimation of the joint's angle. During the experiment described in Section IV-A.1, the resistance of the sensor in compression was also recorded. Because the linear model proved more accurate for Joint C in Section IV-B, this model was chosen for the two sensor angle estimation. A separate linear model was fit for the sensor in tension and the sensor in compression (Fig. 8(a)) based on Eq. (6). The values are given in Table V, along with the correlation coefficients. The fitted models were used individually predict the joint angle as in Section IV-B. As stated in that section, the sensor in tension achieved an RMSE of 5.25°. The sensor in compression achieved an RMSE of 3.84°. The characteristics and resistance of both sensors together were then used to predict the joint angle as well using Eq. (7), achieving an RMSE of 3.13°. The results for a portion of the 3000s total experiment are shown in Fig. 8(b).

C. Joint Control

Without including sensing feedback, open-loop control of a robotic joint is possible. To assess the performance of open-loop control of the robotic joints, an experiment

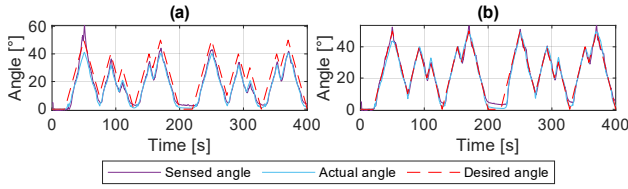


Fig. 10. Desired angle, actual angle, and estimated angle based on sensor input for (a) open-loop control and (b) closed-loop control.

TABLE VI
JOINT CONTROL RESULTS

	Open-Loop Control	Closed-Loop Control
Sensed vs Actual Angle RMSE	1.88°	2.29°
Actual vs Desired Angle RMSE	8.14°	2.92°
Sensed vs Desired Angle RMSE	8.46°	2.93°

was performed using Joint D. Joint D was a unidirectional asymmetric notch joint with design identical to Joint B. The PI model for Joint D was determined using the procedure in Section IV-A.1, with ($N=3$) for the purpose of simplifying the control system. A simple, linear, empirical model relating tendon stroke to joint angle was determined by finding the best fit slope relating these quantities, found to be $m_t=35.49^\circ \text{ mm}^{-1}$. An open-loop control scheme was implemented in Simulink (MathWorks, Natick, MA, USA), where $1/m_t$ was the gain between the desired angle and the commanded tendon stroke given as an input into the low level motor control. The actual ground-truth angle recorded by the EM tracking system and the sensed angle (unused by the controller) was computed according to Section IV-B. These are shown in Fig. 10(a) and the RMSE between them are given in Table VI. A closed-loop control scheme was also implemented for Joint D, a simplified block diagram of which is shown in Fig. 9. In the figure, (a) represents the input desired angle through time. Block (b) is the empirical tendon stroke-joint angle model. Block (c) is the low level motor control. Block (d) represents the physical robot, which is the plant of the system. Block (e) is a PID controller, with proportional, integral, and derivative constants of 0.1 and 0.1, and 0, respectively. Block (f) represents the angle estimation procedure outlined in Section IV-B. The desired angle, actual angle, and estimated angle using the PI model are shown in Fig. 10(b). The RMSE between these values are given in Table VI. The closed-loop control system reduced the tracking error between the actual and desired angle to 2.92° compared to 8.14°, demonstrating the usefulness of the proposed sensors for improving the accuracy of controlling the angle of the robotic joint.

D. Phantom Demonstration

To demonstrate the sensing joint in a tissue-like medium, Joint D was used to navigate inside a hydrogel phantom. The phantom was made of 7% polyvinyl alcohol and 0.85% phytigel (both Sigma-Aldrich, Darmstadt, Germany) solution. A linear translation stage was added to the actuation system for Joint D to allow the advancement of the robotic joint

TABLE VII
DEMONSTRATION RESULTS

	Linear Model	PI Model
Trial 1 RMSE	7.11°	8.17°
Trial 2 RMSE	4.51°	4.51°
Trial 3 RMSE	4.25°	4.18°

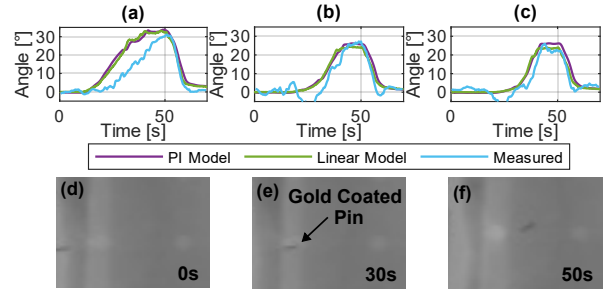


Fig. 11. Data recorded during the hydrogel phantom demonstration for (a) Trial 1, (b) Trial 2, and (c) Trial 3. Sample fluoroscopy images recorded during Trial 2 at timestamps of (d) 0s, (e) 30s, and (f) 50s

into the phantom. An OEC 9800 Plus C-Arm system (GE Healthcare, Chicago, IL, USA) was used to take periodic (2 Hz) fluoroscopic images of the joint to capture the ground truth deflection angle, since using the EM tracker in the hydrogel was not practical. A gold plated pin was affixed to the tip of the robot to increase its visibility under fluoroscopy. The acquired images were cropped, a binary threshold was applied to identify the shape of the pin, and an ellipse was fit to the shape of the pin. The angle between the ellipse's major axis and the horizontal in each image frame was taken to be the joint angle. The values were filtered with a moving average filter of width 8, and the mean value of the angle before bending commenced was subtracted from each angle value to obtain the change in angle. The joint was actuated in a pre-programmed manner while the sensor voltage was recorded. The sensor resistance was calculated and the joint angle estimated using the PI model and linear model obtained in Section IV-C. Three trials were conducted. The angles from the fluoroscopy images and the estimated angles from the sensor are shown in Fig. 11(a), Fig. 11(b), and Fig. 11(c) for Trial 1, Trial 2, and Trial 3, respectively. Selected fluoroscopy image frames before actuation, during bending, and near maximum bending for Trial 2 are shown in Fig. 11(d), Fig. 11(e), and Fig. 11(f), respectively. The RMSE of the PI and linear joint angle estimation for each trial are shown in Table VII. Since the angle estimation from fluoroscopy and the DLW sensor matched closely, the sensor could potentially be used to supplement fluoroscopy guided navigation during a procedure to allow a lower frame rate and therefore decrease exposure for clinicians.

V. CONCLUSION

In this work, a method for fabricating DLW strain sensors directly on polymer notched-tube robotic joints was proposed and demonstrated. The fabricated sensing joints were characterized using both linear and nonlinear approaches. Rate

dependence and relaxation were considered. The sensors were used to estimate the angle of the sensing joints, and it was shown that the sensor feedback could be used to implement closed-loop control. Finally, a demonstration of a sensing joint in a hydrogel phantom was presented. While the experiments showed low errors in estimating the bending angle and low tracking errors during closed-loop control, the sensing joints have opportunities for improvement. The sensing range is relatively low, with saturation observed at less than 2% strain. Additionally, the durability and temperature dependence of the sensors will need to be investigated further. Future work will also compare the performance of the proposed sensor to other shape sensing methods. Overall, the integration of DLW sensors directly onto continuum robotic joints represents a low-cost, easily fabricated method to obtain shape feedback.

REFERENCES

- [1] C. Shi, X. Luo, P. Qi, T. Li, S. Song, Z. Najdovski, T. Fukuda, and H. Ren, "Shape Sensing Techniques for Continuum Robots in Minimally Invasive Surgery: A Survey," *IEEE Transactions on Biomedical Engineering*, vol. 64, no. 8, pp. 1665–1678, 8 2017.
- [2] P. Sincak, E. Prada, L. Mikova, R. Mykhailyshyn, M. Varga, T. Merva, and I. Virgala, "Sensing of Continuum Robots: A Review," *Sensors*, vol. 24, no. 4, p. 1311, 2 2024.
- [3] O. Erin, M. Boyvat, M. E. Tiryaki, M. Phelan, and M. Sitti, "Magnetic Resonance Imaging System-Driven Medical Robotics," *Advanced Intelligent Systems*, vol. 2, no. 2, 2 2020.
- [4] C. Zhang, Y. Lu, S. Song, and M. Q.-H. Meng, "Shape tracking and navigation for continuum surgical robot based on magnetic tracking," in *2017 IEEE International Conference on Information and Automation (ICIA)*. IEEE, 7 2017, pp. 1143–1149.
- [5] J. Wang, Y. Lu, C. Zhang, S. Song, and M. Q.-H. Meng, "Pilot study on shape sensing for continuum tubular robot with multi-magnet tracking algorithm," in *2017 IEEE International Conference on Robotics and Biomimetics (ROBIO)*. IEEE, 12 2017, pp. 1165–1170.
- [6] Y.-L. Park, S. Elayaperumal, B. Daniel, S. C. Ryu, M. Shin, J. Savall, R. J. Black, B. Moslehi, and M. R. Cutkosky, "Real-Time Estimation of 3-D Needle Shape and Deflection for MRI-Guided Interventions," *IEEE/ASME Transactions on Mechatronics*, 12 2010.
- [7] J. Sheng, N. J. Deaton, and J. P. Desai, "A Large-Deflection FBG Bending Sensor for SMA Bending Modules for Steerable Surgical Robots," in *2019 International Conference on Robotics and Automation (ICRA)*. IEEE, 5 2019, pp. 900–906.
- [8] G. Gerboni, A. Diodato, G. Ciuti, M. Cianchetti, and A. Menciasci, "Feedback Control of Soft Robot Actuators via Commercial Flex Bend Sensors," *IEEE/ASME Transactions on Mechatronics*, vol. 22, no. 4, pp. 1881–1888, 8 2017.
- [9] Q. Zhao, J. Lai, K. Huang, X. Hu, and H. K. Chu, "Shape Estimation and Control of a Soft Continuum Robot Under External Payloads," *IEEE/ASME Transactions on Mechatronics*, vol. 27, no. 5, pp. 2511–2522, 10 2022.
- [10] Y. Chen, J. M. Oliveira, and I. W. Hunter, "Two-axis bend sensor design, kinematics and control for a continuum robotic endoscope," in *2013 IEEE International Conference on Robotics and Automation*. IEEE, 5 2013, pp. 704–710.
- [11] L. Pan, T. Zhang, Y. Cheng, Z. Ma, and J. Li, "Shape Sensing for Continuum Robots Based on MWCNTs-PDMS Flexible Resistive Strain Sensors," *IEEE Transactions on Medical Robotics and Bionics*, vol. 7, no. 3, pp. 1286–1296, 8 2025.
- [12] D. C. Moyer, W. Wang, L. S. Karschner, L. Fichera, and P. M. Rao, "Fabrication and Characterization of Additively Manufactured Stretchable Strain Sensors Towards the Shape Sensing of Continuum Robots," *IEEE Robotics and Automation Letters*, vol. 10, no. 7, pp. 7627–7634, 7 2025.
- [13] D. Alatorre, D. Axinte, and A. Rabani, "Continuum Robot Proprioception: The Ionic Liquid Approach," *IEEE Transactions on Robotics*, vol. 38, no. 1, pp. 526–535, 2 2022.
- [14] N. Malhotra, K. Hoang, and J. P. Desai, "Design, fabrication, and packaging of a piezoresistive MEMS-based force sensor on a steerable probe: Towards brain tumor margin identification," *Sensors and Actuators A: Physical*, vol. 377, p. 115702, 10 2024.
- [15] H. J. Pandya, J. Sheng, and J. P. Desai, "Towards a tri-axial flexible force sensor for catheter contact force measurement," in *2016 IEEE SENSORS*. IEEE, 10 2016, pp. 1–3.
- [16] R. Srinivasan, R. Hall, W. Wilson, W. Loehle, and D. Allbee, "Ultraviolet laser irradiation of the polyimide, PMDA-ODA (Kapton™), to yield a patternable, porous, electrically conducting carbon network," *Synthetic Metals*, vol. 66, no. 3, pp. 301–307, 10 1994.
- [17] J. Lin, Z. Peng, Y. Liu, F. Ruiz-Zepeda, R. Ye, E. L. G. Samuel, M. J. Yacaman, B. I. Jakobson, and J. M. Tour, "Laser-induced porous graphene films from commercial polymers," *Nature Communications*, vol. 5, no. 1, p. 5714, 12 2014.
- [18] R. K. Biswas, N. Farid, B. B. Bhatt, D. Gupta, G. M. O'Connor, and P. Scully, "Femtosecond infra-red laser carbonization and ablation of polyimide for fabrication of Kirigami inspired strain sensor," *Journal of Physics D: Applied Physics*, vol. 56, no. 8, p. 085101, 2 2023.
- [19] X. Duan, Y. Yao, M. Niu, J. Luo, R. Wang, and T. Liu, "Direct Laser Writing of Functional Strain Sensors in Polyimide Tubes," *ACS Applied Polymer Materials*, vol. 1, no. 11, pp. 2914–2923, 11 2019.
- [20] A. K. Rothe, N. Malhotra, C. C. Barré, and J. P. Desai, "Towards Shape Estimation of Meso-Scale Continuum Robots Using Direct Laser Written Piezoresistive Strain Sensors," in *2025 International Symposium on Medical Robotics (ISMR)*. IEEE, 5 2025, pp. 108–114.
- [21] N. Malhotra, A. K. Rothe, R. Konda, and J. P. Desai, "Design of a Polymer-Based Steerable Cannula for Neurosurgical Applications," in *Proceedings of the 14th Conference on New Technologies for Computer/Robot Assisted Surgery*, Lisbon, Portugal, 10 2025, pp. 103–104.
- [22] A. K. Rothe, T. A. Brumfiel, R. Konda, K. M. Williams, and J. P. Desai, "Model-based Parameter Selection for a Steerable Continuum Robot — Applications to Bronchoalveolar Lavage (BAL)," *IEEE Robotics and Automation Letters*, 11 2024.
- [23] A. M. Barja, Y. K. Ryu, S. Tarancón, E. Tejado, A. Hamada, A. Velasco, and J. Martínez, "Laser-Induced Graphene Strain Sensors for Body Movement Monitoring," *ACS Omega*, vol. 9, no. 37, pp. 38 359–38 370, 9 2024.
- [24] A. F. Carvalho, A. J. S. Fernandes, C. Leitão, J. Deuermeier, A. C. Marques, R. Martins, E. Fortunato, and F. M. Costa, "Laser-Induced Graphene Strain Sensors Produced by Ultraviolet Irradiation of Polyimide," *Advanced Functional Materials*, vol. 28, no. 52, 12 2018.
- [25] T. G. Beckwith, N. L. Buck, and R. D. Marangoni, *Mechanical Measurements*, ser. Addison-Wesley series in mechanical engineering. Addison-Wesley Publishing Company, 1982.
- [26] Y. Wang, X. Li, X. Xu, G. Li, S. Xuan, X. Li, and K. Yin, "A flexible piezoresistive three-dimensional strain sensor based on laser-induced graphene/nanosilver/MWCNTs for precise human all-range motion detection," *Applied Physics Letters*, vol. 126, no. 2, 1 2025.
- [27] L. Huang, H. Wang, P. Wu, W. Huang, W. Gao, F. Fang, N. Cai, R. Chen, and Z. Zhu, "Wearable Flexible Strain Sensor Based on Three-Dimensional Wavy Laser-Induced Graphene and Silicone Rubber," *Sensors*, vol. 20, no. 15, p. 4266, 7 2020.
- [28] X. Chen, K. W. Gan, S. H. Pu, M. Jalalvand, and A. R. Hamilton, "Piezoresistive laser-induced graphene as a low-cost strain sensor for composite structures," *Sensors and Actuators A: Physical*, vol. 393, p. 116776, 10 2025.
- [29] M. Al Janaideh, M. Al Saaideh, and X. Tan, "The Prandtl-Ishlinskii Hysteresis Model: Fundamentals of the Model and Its Inverse Compensator [Lecture Notes]," *IEEE Control Systems*, vol. 43, no. 2, pp. 66–84, 4 2023.
- [30] K. Bhole and S. Sondkar, "Identification of Prandtl-Ishlinskii Hysteresis Model and Its Inverse for Varying Hysteresis Nonlinearities," in *2018 9th IEEE Control and System Graduate Research Colloquium (ICSGRC)*. IEEE, 8 2018, pp. 69–74.
- [31] A. S. Thakur, S. Dubey, S. Kumar, A. S. Thakur, and R. Vaish, "Engineered mechanically exfoliated flexible graphene-based frugal strain sensors," *Chemical Engineering Journal*, vol. 504, p. 158839, 1 2025.
- [32] E. Krempl and F. Khan, "Rate (time)-dependent deformation behavior: an overview of some properties of metals and solid polymers," *International Journal of Plasticity*, vol. 19, no. 7, pp. 1069–1095, 7 2003.